Contrib Mineral Petrol (1996) 126: 181 – 198

Leander Franz · Gerhard P. Brey · Martin Okrusch

Steady state geotherm, thermal disturbances, and tectonic development of the lower lithosphere underneath the Gibeon Kimberlite Province, Namibia

Received: 8 March 1996 / Accepted: 5 August 1996

Abstract The Gibeon Kimberlite Province of southern Namibia comprises more than 75 group 1 kimberlite pipes and dykes. From the Gibeon Townsland 1 pipe, 38 upper mantle xenoliths (23 garnet lherzolites and 15 garnet harzburgites) were collected and minerals were analysed by electron microprobe for major elements. Pressures and temperatures of crystallisation for xenoliths with either coarse equant, porphyroclastic and mosaic-porphyroclastic textures were estimated by a number of combinations of geothermometers and geobarometers judged to be reliable and accurate for peridotites by Brey and Köhler (1990): The *P-T* estimates for equilibrated xenoliths agree within the errors of the methods and plot within the stability field of graphite. The *P-T* values for coarse equant xenoliths fall close to a geothermal gradient of about 44 mW/m^2 within a very restricted pressure range. The porphyroclastic xenoliths yield similar and higher temperatures at similar depths. In these xenoliths Ca in orthopyroxene and Ca in olivine increase towards the rims and are high in the neoblasts indicating a stage of transient heating at depth. The mosaic-porphyroclastic xenolith minerals yield the highest temperatures, are unzoned and indicate internal mineral equilibrium. The depth of origin for the xenoliths from Gibeon Townsland 1 ranges from 100 to 140 km. The "cold", coarse equant peridotites are relatively enriched garnet lherzolites with comparatively (to the "hot" peridotites) low modal orthopyroxene contents, whereas the "hot", mosaic-porphyroclastic peridotites are depleted garnet harzburgites with high modal amounts of orthopyroxene. This is opposite to the findings for peridotites from the Kaapvaal craton where the cold peridotites are depleted harzburgites with high modal orthopyroxene and many of the hot peridotites are fertile lherzolites with low modal abundance of orthopyroxene. We present a model in which the high temperature, depleted garnet harzburgites are equated to the cold, coarse equant peridotites from the Kaapvaal craton. It is envisaged that this material was detached and transported laterally by an upwelling, deflected plume.

L. Franz (✉)[1*] · M. Okrusch
Mineralogisches Institut der Universität Würzburg,
Am Hubland, D-97074 Würzburg, Germany

G. P. Brey
Institut für Geochemie und Petrologie,
J.W. Goethe-Universität, Senckenberganlage 28,
D-60054 Frankfurt, Germany

**Present address*:
GeoForschungsZentrum Potsdam,
Telegrafenberg, D-14473 Potsdam, Germany

Editorial responsibility: W. Schreyer

Introduction

The Gibeon Kimberlite Province (Namibia) consists of a large number of garnet lherzolite bearing, apparently non-diamondiferous kimberlite dikes and diatremes, carbonatites and monticellite picrites. Earlier studies (MacGregor 1975; Mitchell 1984) on garnet peridotites from two pipes (Hanaus and Louwrensia) indicate a shallower origin for these mantle samples compared to those from the "on-craton" kimberlites of the Kaapvaal craton. We have collected a cd\new suite of xenoliths from the polyintrusive Gibeon Townsland 1 pipe which yielded a great number of very fresh and unaltered xenoliths in three different kimberlite facies. The comparison of the petrology, the deformation features and the mineral chemistry, and the application of newly evaluated and calibrated geothermobarometers (Brey et al. 1990; Brey and Köhler 1990) to this xenolith suite and the published data from Hanaus and Louwrensia should enable us to discern similarities and differences between the upper mantle beneath the younger crustal segments of the Gibeon Kimberlite Province and the much older crustal segments of the Kaapvaal craton.

Regional geology and geological setting

The Gibeon Kimberlite Province of southern Namibia is located between Keetmanshoop and Mariental within the Precambrian to Cambrian Nama subgroup in a 1.6–2.0 Ga old crustal segment (Hartnady et al. 1985; Hoal et al. 1995). The province extends from the Brukkaros mountain over 110 km in NS- and about 70 km in EW-direction (Fig. 1). It comprises the ultramafic complex of the Blue Hills, the enigmatic Gross Brukkaros (Stachel et al. 1994), more than 75 kimberlite pipes and dykes and, in addition, a substantial number of carbonatite dikes and diatremes (Janse 1964, 1971, 1975; Kurszlaukis 1994; Kurszlaukis et al. 1995; Lorenz et al. 1995). The kimberlites are dominantly group 1 kimberlites according to the classification scheme of Smith (1983) and erupted 70–80 Ma ago (Spriggs 1988). These "off-craton" kimberlites are apparently non-diamondiferous unlike the older "on-craton" kimberlites of the adjacent Kaapvaal craton (Clifford 1966). Isotopic investigations suggest that these kimberlites may be related to the Vema hot spot, which is now active in the Atlantic ocean (Spriggs 1988).

The investigated mantle xenoliths were collected from the hypabyssal Gibeon Townsland 1 diatreme, the largest pipe of the Gibeon Kimberlite Province. Its shape indicates a NNE–SSW trending fissure eruption with a length of more than 470 m and a width of 40–100 m (Fig. 2). The pipe lies within shales and quartzites of the Cambrian to Precambrian Nama subgroup and, at the southern end, within Dwyka boulder shales and quartzites of Karroo age. The Nama sediments are uplifted and slightly metamorphosed at the contact to the pipe. Three different kimberlitic facies can be distinguished, which indicates a polyphase intrusion typical of all kimberlites:

1. Facies "A" (A for Autoliths) is a brownish kimberlite at the southern end of the pipe with numerous autoliths (pelletal lapilli in the nomenclature of Clement and Skinner 1985) ranging in diameter from 0.2 to 4 cm in a fine grained matrix. The facies contains very few xenoliths.

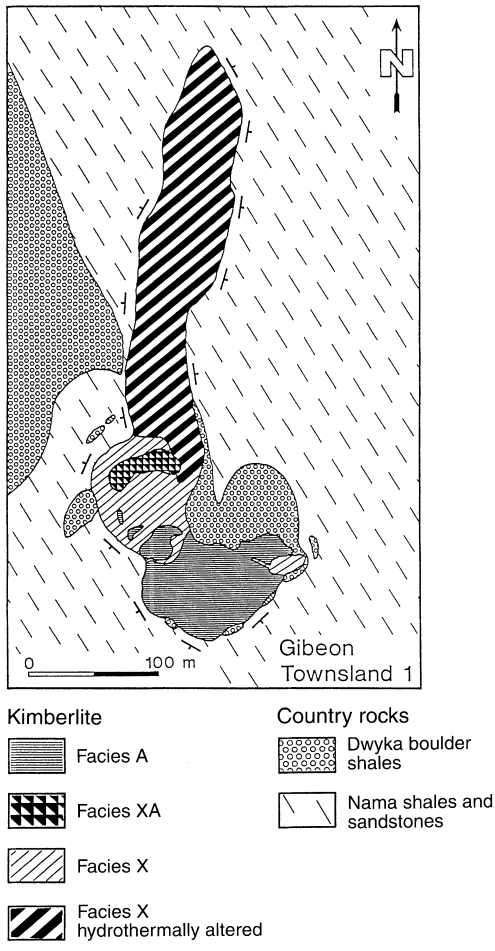

Fig. 2 Geological scetch map of the Gibeon Townsland 1 pipe

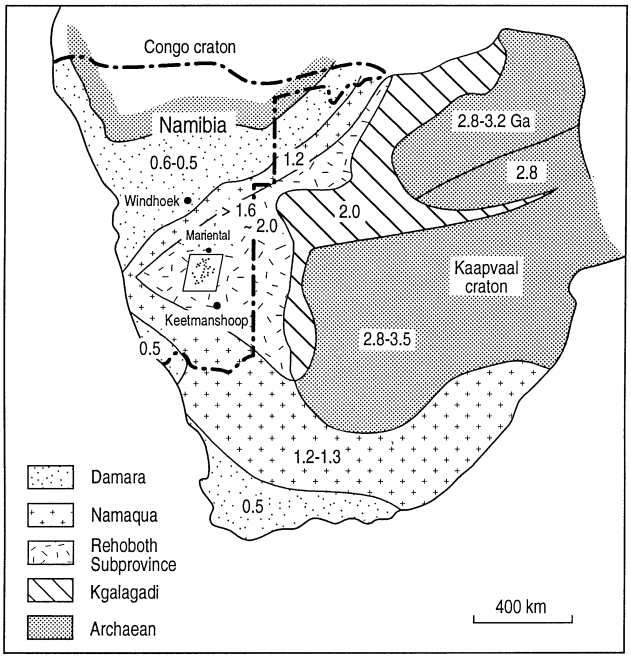

Fig. 1 Position of the Gibeon Kimberlite Province (enclosed) in Southern Africa after Hartnady et al. (1985)

2. Facies "XA" (XA for Xenoliths and Autoliths) in the centre of the diatreme contains only very few autoliths and is very rich in garnet peridotite xenoliths.
3. The major part of the diatreme is formed by facies "X" (X for Xenoliths only). It is intensively altered by hydrothermal solutions with carbonatisation and zeolitisation mainly in the northern part. The dark greyish rock contains a huge amount of crustal as well as mantle xenoliths and, in the northern part, big blocks (up to 2 m) of dolerite. Facies "X" represents the oldest magmatic event as indicated by cutting dykes of facies "A" and xenoliths of facies "X" within facies "A" and "XA". The three facies are very similar in major and trace element contents (see Table 1) and probably represent different pulses of the same magma.

Analytical methods and procedures

Mineral analyses were carried out with a CAMECA SX 50 electron beam microprobe with four spectrometers. Major and minor elements were determined at 15 kV acceleration voltage and a beam current of 10 nA and with counting times of 20 seconds for Si, Al, Mg, Ca and K, 30 seconds for Fe and Ni, and 40 seconds for Na, Cr, Mn and Ti. The CAMECA standard set was used for reference and the PAP program for matrix correction. In each thin section, three different grains of grt, ol, opx and, if present, cpx were measured with 3–6 points from core to rim. In 9 selected samples, Ca was determined in olivine with the trace element program of CAMECA with wollastonite as a standard. Counting time was

Table 1 XRF analyses of Gibeon Townsland 1 kimberlite facies "X", "A" and "XA" and microprobe analyses of melt inclusions in the recrystallized rims of clinopyroxenes (n.d. not determined)

Kimberlites:							Melt inclusions in cpx:				
Sample no.:	KGG105	KGG107	KGG109	KGG110	KGG103	KGG100	KGG48	KGG48	KGG48	KGG48	KGG48
Facies:	X	X	A	A	XA	XA	INCL1	INCL4	INCL5	INCL6	INCL7
Oxides (wt%)											
SiO_2	35.98	36.17	35.70	33.16	31.11	30.36	38.27	35.41	42.67	41.34	42.60
TiO_2	0.81	0.92	1.05	1.06	1.05	1.04	0.19	2.92	1.40	0.10	0.16
Al_2O_3	4.13	3.43	2.11	2.41	2.03	1.98	5.90	6.59	6.36	6.08	5.91
Fe_2O_3	6.41	6.27	6.82	7.14	7.84	7.27	-	-	-	-	-
Cr_2O_3	0.22	0.22	0.26	0.22	0.24	0.27	0.29	3.47	0.48	0.23	0.23
FeO	1.39	1.37	1.12	1.03	0.65	0.94	9.86	10.19	8.19	6.63	7.90
MnO	0.15	0.15	0.16	0.16	0.16	0.16	0.19	0.25	0.10	0.14	0.10
MgO	32.08	32.29	32.81	31.49	31.82	1.34	25.46	28.17	21.78	33.09	30.06
CaO	4.87	5.15	5.91	7.65	7.57	8.08	9.00	0.95	10.33	0.45	0.33
Na_2O	0.11	0.12	0.18	0.20	0.30	0.19	0.17	0.17	0.24	0.25	0.14
K_2O	0.69	0.89	0.04	0.04	0.02	0.05	0.68	2.18	2.95	2.15	3.47
P_2O_5	0.39	0.55	0.91	0.44	0.43	0.51	n.d.	n.d.	n.d.	n.d.	n.d.
H_2O	11.37	10.79	12.70	10.68	10.93	10.85	n.d.	n.d.	n.d.	n.d.	n.d.
CO_2	0.62	1.14	n.d.	4.30	5.13	5.64	n.d.	n.d.	n.d.	n.d.	n.d.
SO_2	0.03	0.01	n.d.	0.03	0.02	0.02	n.d.	n.d.	n.d.	n.d.	n.d.
Total:	99.24	99.47	99.76	100.00	99.29	98.69	90.01	90.30	94.50	90.48	90.90
Trace elements (ppm)											
V	57	127	82	80	47	280					
Co	95	92	77	90	79	87					
Ni	1428	1376	1263	1272	1339	1299					
Zn	61	53	54	48	51	50					
Ga	10	12	9	10	6	13					
Rb	58	52	9	8	6	12					
Sr	836	584	865	724	597	951					
Y	9	9	8	10	10	11					
Zr	131	134	151	155	148	155					
Nb	102	119	155	135	138	145					
Mo	<5	<5	<5	<5	<5	<5					
Sn	<15	<15	<15	<15	<15	<15					
Ba	1698	1787	1246	972	885	1378					
Pb	8	10	<5	<5	8	8					
Th	14	16	20	19	17	26					
U	<5	9	7	<5	<5	8					

300 s, acceleration voltage 20 kV and beam current 50 nA. The accuracy of the analyses was checked with the olivine SC/KA (Köhler and Brey 1990) which contains 524 (±5) ppm Ca.

All mineral analyses were performed in the central parts of the xenoliths to avoid alteration zones at the rims. Mineral formulas for garnets calculated on the basis of 24 oxygens result in totals of cations from 15.99 to 16.04. This variation lies within the range of analytical error, which makes the calculation of Fe^{3+} from the structural formula meaningless (see also Luth et al. 1990). Orthopyroxenes and the cores of clinopyroxenes reveal totals of cations from 3.89–4.01 on the basis of 6 oxygens, which refutes a calculation of Fe^{3+}. The sum of cations in the serrated rims of clinopyroxenes is higher indicating prominent amounts of Fe^{3+} (see below). Mineral abbreviations used in this publication are taken from Kretz (1983).

Petrography and mineral chemistry of the xenoliths

Thirty-eight garnet peridotite xenoliths were selected for detailed investigation, from which 6 originated from facies "A", 14 from facies "XA" and 18 from facies "X". The size of the xenoliths ranged from 2–10 cm in diameter with only very little weathering or alteration at the rims. All samples were examined in polished thin sections, both in transmitted and reflected light. The modal composition of the samples was determined with a Swift point counter with 1500 points in a normal sized thin section (see Table 2). The textural classification of the samples is according to the scheme of Harte (1977). We distinguish three textural types: coarse equant (CE), porphyroclastic (P) and mosaic-porphyroclastic (MP) xenoliths.

Coarse equant xenoliths (CE)

Eighteen samples show coarse equant textures with polygonal to slightly curved grain boundaries. All minerals have a granular shape and have diameters of more than 2 mm with garnets usually exceeding 5 mm. Garnets of the CE xenoliths have small kelyphitic rims of orthopyroxene, clinopyroxene and spinel. These rims, which hardly exceed 0.5 mm in size, are suggested to have formed during uplift by the kimberlite as shown for xenoliths of the adjacent Hanaus and Anis Kubub pipes (Franz et al. 1996). The CE xenoliths show no recrystallisation and the only deformation textures re-

cognized are undulous extinctions and cataclastic fracturing of the minerals (see Fig. 4a). Sixteen coarse equant xenoliths are garnet lherzolites and two are garnet harzburgites. Modal olivine contents range from 55 to 80 vol.% (Fig. 3), orthopyroxene from 5 to 25 vol.% with a pronounced maximum between 10–15 vol.%, clinopyroxene from 2.5 to almost 20 vol.% and garnet from 2.5 to 17.5 vol.%.

Garnets are homogeneous and display X_{Mg}-values [= Mg/(Mg+Fe)] of 0.80–0.84, X_{Cr} [= Cr/(Cr+Al)] of 0.07–0.16 and X_{Ca} [= Ca/(Ca+Mg+Mn+Fe)] of 0.12–0.15 (Table 3). Some garnets are zoned with X_{Mg} increasing from 0.82–0.84 from core to rim at the expense of Fe (e.g. samples KGG20A and KGG31 in Table 3). In some cases distinct variations in X_{Cr} are recorded in different garnets from the same sample (see KGG63 in Table 3).

The granoblastic to short prismatic, colourless to faintly brown orthopyroxenes are homogeneous with $En_{91.5–93.2}$ (Table 4). In two samples (e.g. KGG63 in

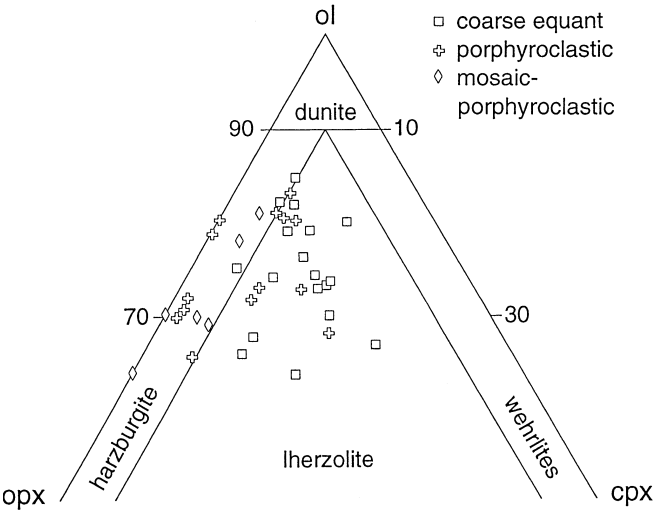

Fig. 3 Normalized ol-opx-cpx diagram for the xenoliths from the Gibeon Townsland 1 pipe

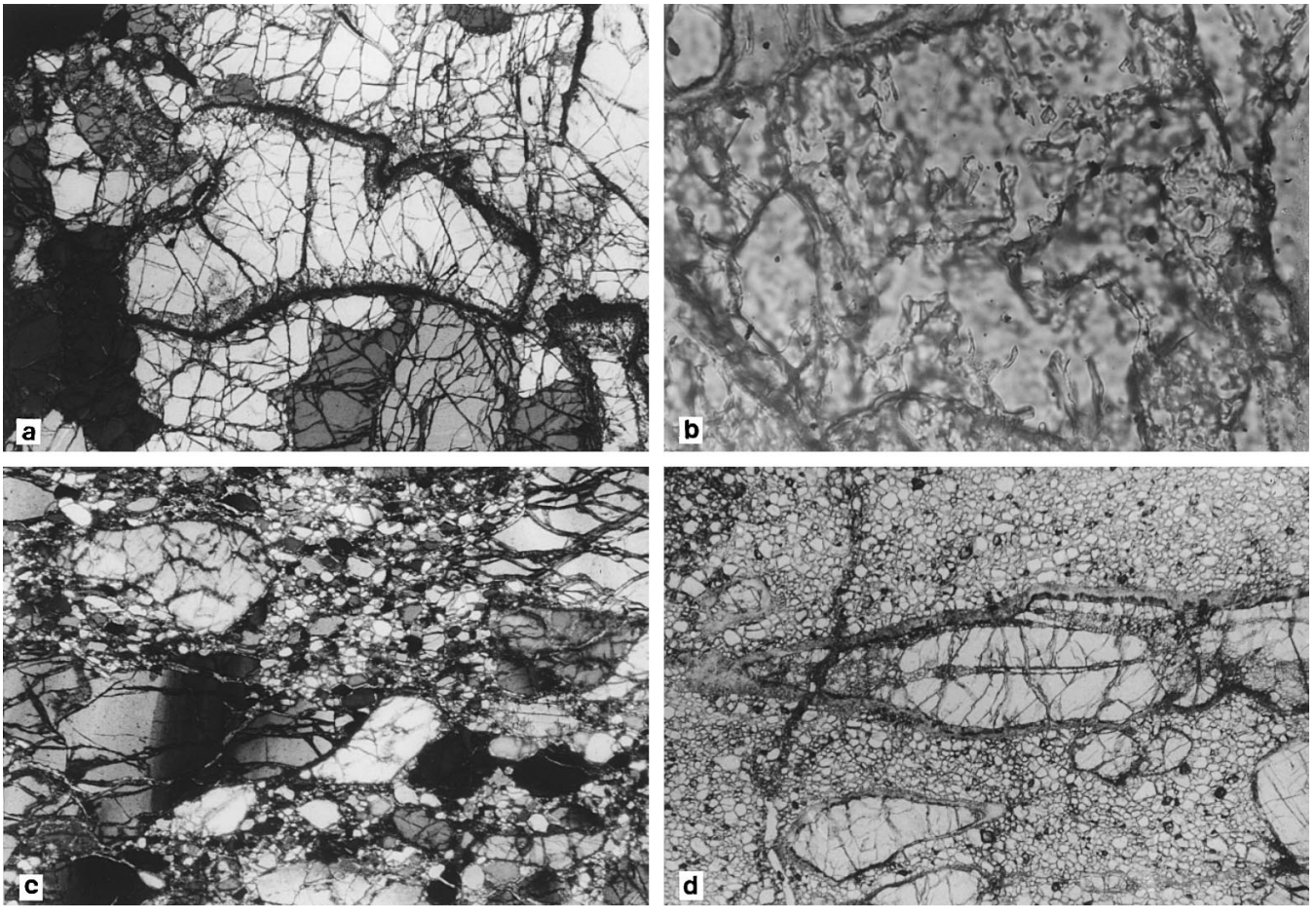

Fig. 4a-d Microphotographs of the various xenolith types: **a** coarse equant xenolith with granoblastic orthopyroxene, olivine and zoned clinopyroxene (crossed polarizers); *length* of photograph: 7.8 mm; **b** detail of rim section of zoned clinopyroxene (cp. Fig. 4a) with small melt inclusions (parallel polarizers); **c** porphyroclastic xenolith with clinopyroxene, undulous olivine porphyroclasts and neoblasts (crossed polarizers); *length* of photograph: 4.3 mm; **d** mosaic-porphyroclastic xenolith with elongated orthopyroxenes in a matrix of dynamically recrystallized olivine (parallel polarizers); *length* of photograph: 4.3 mm

Table 2 Textures (*CE* = coarse equant, *P* = porphyroclastic, *MP* = mosaic-porphyroclastic), facies of the kimberlite host, and modal mineralogy of the investigated xenoliths; samples are arranged in the order of decreasing cpx contents

Sample	Texture	Facies	Modal mineralogy			
			Ol	Opx	Cpx	Grt
KGG31	CE	A	57	10	18	15
KGG16	P	XA	66	15	15	4
KGG63	CE	X	60	21	14	6
KGG13	CE	XA	68	13	12	6
KGG45	CE	X	59	13	12	17
KGG23	CE	A	63	11	12	14
KGG20B	CE	X	64	12	11	12
KGG14	CE	XA	63	11	10	16
KGG62	CE	X	67	7	10	16
KGG30	P	A	65	14	10	12
KGG66	CE	X	68	12	9	11
KGG54	CE	X	62	23	9	7
KGG06	CE	XA	73	11	9	8
KGG20A	CE	X	58	19	7	16
KGG50	CE	X	65	16	7	12
KGG70	P	XA	77	12	7	4
KGG81	P	XA	68	19	7	6
KGG48	P	X	67	18	7	8
KGG72	CE	XA	76	14	6	4
KGG62A	P	X	76	13	5	6
KGG83	CE	XA	79	9	5	7
KGG77	P	XA	77	13	5	5
KGG55	P	X	81	11	5	3
KGG71	MP	XA	67	26	5	2
KGG60	CE	X	67	10	5	18
KGG36	P	A	63	28	4	5
KGG65	CE	X	76	12	4	7
KGG88	CE	XA	72	20	4	4
KGG69	MP	XA	78	16	3	3
KGG56	MP	X	74	18	3	5
KGG44a	MP	A	56	23	2	19
KGG65a	P	X	69	28	1	2
KGG68	P	XA	68	26	1	6
KGG37	P	A	63	27	<1	10
KGG46	MP	X	57	24	0	19
KGG51	P	X	74	19	0	7
KGG52	MP	X	62	35	0	3
KGG84	P	XA	76	20	0	3

Table 4), Al slightly increases from core to rim and in two other samples (see KGG20B and KGG72 in Table 4) Al and Ca in orthopyroxene vary from grain to grain without any discernible zonation patterns.

A strong discontinuous zonation is developed in many clinopyroxenes: the granoblastic and short prismatic chromian diopsides with faint green absorption colours and a mean length of about 3 mm have serrated and embayed rims (Fig. 4 a,b) with numerous fine melt inclusions of ultrabasic glass (see below). These rims have a width of 0.1–1 mm and show, compared to the homogeneous interior, a sharp decrease in Na, a slight decrease in Al, and an increase in Ca (see Fig. 5 and samples KGG72 and KGG88 in Table 5). Totals of cations in these clinopyroxene rims are commonly greater than four (4.01–4.03) indicating ferric iron of 30–100% of total iron. The maximum size of the melt inclusions does not exceed 10 micrometers, which renders it impossible to obtain high quality microprobe analyses: neither can incorporation of adjacent clinopyroxene into the analysis be avoided nor the loss of Na and K during the analysis because of the strongly focused electron beam. Nevertheless, ultrabasic composition can be discerned from the analyses given in Table 1, which may indicate that this reaction rim developed by contact with melt or fluid phase at mantle depth.

Olivines of the coarse equant xenoliths are homogeneous with $Fo_{90.4–92.4}$ and Ca ranging from 200–250 ppm (Tables 6 and 7; Figs. 5 and 6). In only one sample (KGG50; see Table 6) do olivine compositions vary from grain to grain ($Fo_{90.4–91.2}$) and in a few instances Ca increases near rims adjacent to the zoned clinopyroxenes.

Porphyroclastic xenoliths (P)

Fourteen samples have relatively large, distinctly strained olivine porphyroclasts rimmed by small re-

Table 3 Representative microprobe analyses of garnets (wt%; *c* core, *r* rim). Legend of the samples see Table 2

	KGG31 Grt c	KGG31 Grt r	KGG16 Grt c	KGG63 Grt1 c	KGG63 Grt2 c	KGG63 Grt3 c	KGG13 Grt c	KGG45 Grt c	KGG23 Grt c	KGG208 Grt c	KGG14 Grt c
SiO_2	41.58	41.39	41.48	41.52	41.61	41.26	41.59	41.97	41.70	41.95	41.96
TiO_2	0.21	0.19	0.17	0.29	0.29	0.36	0.08	0.28	0.11	0.014	0.27
Al_2O_3	19.71	19.82	20.71	21.62	21.98	20.81	20.98	21.25	19.81	21.59	21.66
Cr_2O_3	4.71	4.70	3.66	2.42	2.0	3.34	4.09	2.74	5.43	2.83	2.66
MgO	20.32	20.31	20.11	20.42	20.47	19.72	20.29	20.37	19.64	20.50	20.19
CaO	5.33	5.44	5.40	4.73	4.64	5.05	5.40	4.72	5.80	5.07	4.89
MnO	0.45	0.40	0.34	0.41	0.39	0.37	0.37	0.48	0.40	0.37	0.38
FeO	7.37	6.88	7.12	8.02	8.32	8.62	7.75	8.18	7.97	8.08	7.98
Total:	99.68	99.13	99.99	99.43	99.68	99.54	100.55	100.00	100.87	100.53	99.98
	KGG62 Grt c	KGG30 Grt c	KGG66 Grt c	KGG54 Grt c	KGG06 Grt c	KGG20A Grt c	KGG20A Grt r	KGG50 Grt c	KGG70 Grt c	KGG81 Grt c	KGG48 Grt c
SiO_2	41.39	41.53	40.86	41.36	41.59	41.99	41.93	42.14	40.79	41.28	41.50
TiO_2	0.42	0.25	0.23	0.33	0.31	0.11	0.12	0.07	0.24	0.18	0.19
Al_2O_3	19.47	21.66	21.50	21.80	20.66	21.22	21.73	21.54	21.56	19.99	20.18
Cr_2O_3	5.43	2.67	2.82	2.51	3.34	2.81	2.61	2.67	2.94	4.94	4.57
MgO	19.35	20.57	20.23	20.31	19.93	20.41	20.91	20.70	20.50	20.12	20.93
CaO	5.69	4.99	4.88	4.77	4.90	5.31	4.92	4.84	5.03	5.32	5.41
MnO	0.44	0.35	0.40	0.38	0.38	0.36	0.37	0.43	0.43	0.39	0.35
FeO	8.45	8.06	8.29	8.20	8.02	7.87	7.21	7.73	8.05	7.68	6.50
Total:	100.65	100.08	99.21	99.65	99.12	99.91	99.80	100.12	99.53	99.90	99.64
	KGG72 Grt c	KGG62A Grt c	KGG62A Grt r	KGG83 Grt c	KGG77 Grt c	KGG55 Grt c	KGG55 Grt r	KGG71 Grt c	KGG60 Grt c	KGG36 Grt c	KGG65 Grt c
SiO_2	41.58	42.28	42.39	41.13	41.19	42.29	41.95	41.89	40.80	41.37	40.82
TiO_2	0.18	0.18	0.18	0.23	0.09	0.21	0.17	0.81	0.25	0.13	0.29
Al_2O_3	19.85	20.95	20.77	19.45	19.96	21.80	22.29	18.87	21.81	20.39	20.06
Cr_2O_3	4.44	3.96	4.16	4.79	5.21	2.60	2.31	5.76	2.42	4.47	4.56
MgO	19.50	21.00	21.22	19.52	19.95	20.57	21.31	20.66	20.37	19.67	20.04
CaO	5.61	5.06	5.21	5.57	5.90	4.80	4.77	6.26	4.89	5.41	5.42
MnO	0.46	0.40	0.30	0.43	0.44	0.39	0.27	0.29	0.44	0.34	0.39
FeO	7.95	7.18	6.51	7.09	7.47	8.05	7.24	5.88	8.17	6.76	7.56
Total:	99.57	101.00	100.74	98.21	100.22	100.72	100.31	100.42	99.15	98.54	99.14
	KGG88A Grt c	KGG69 Grt c	KGG56 Grt r	KGG44A Grt r	KGG65A Grt c	KGG68 Grt c	KGG37 Grt c	KGG46 Grt c	KGG51 Grt c	KGG52 Grt r	KGG84 Grt c
SiO_2	41.39	41.08	41.70	41.24	41.11	41.12	41.94	41.48	41.84	41.61	41.55
TiO_2	0.29	0.14	0.40	0.12	0.29	0.16	0.20	0.16	0.16	0.34	0.04
Al_2O_3	20.66	20.11	20.56	22.66	19.38	19.13	19.95	21.23	19.70	18.62	18.45
Cr_2O_3	4.07	5.02	4.52	2.46	5.81	6.25	5.20	3.73	5.26	6.77	7.18
MgO	19.52	21.41	21.42	21.23	20.75	20.11	20.31	21.51	21.07	20.38	21.80
CaO	5.19	5.42	5.36	4.90	5.85	6.32	5.55	5.47	5.70	5.95	4.50
MnO	0.39	0.26	0.29	0.34	0.48	0.45	0.39	0.28	0.30	0.38	0.27
FeO	7.45	6.10	6.34	7.20	6.09	6.35	7.00	5.62	5.62	6.08	5.45
Total:	98.95	99.52	100.60	100.16	100.76	99.88	99.53	100.48	99.64	99.13	99.24

crystallized neoblasts (see Fig. 4c). The diameter of the porphyroclasts varies between 1 and 4 mm whereas the neoblasts never exceed 0.2 mm. The olivine neoblasts may comprise up to 70 vol.% of the total amount of olivine. Neoblasts of orthopyroxene are rare, and clinopyroxene and garnet do not show any recrystallisation. Beside this dynamic recrystallisation, the xenoliths are intensively fractured. Seven of the investigated samples are garnet harzburgites and the other seven garnet lherzolites (Fig. 3).

Garnets from porphyroclastic xenoliths have similar grain sizes and are often chemically similar to garnets from the coarse equant xenoliths except for somewhat higher Cr and Mg contents; they reveal X_{Mg}-values of 0.81–0.87, X_{Cr} of 0.07–0.18 and X_{Ca} of 0.12–0.16. Some garnets display a slight increase of Mg towards the rim (e.g. samples KGG55 and KGG62A in Table 3). In one harzburgitic sample (KGG84), subcalcic garnet, i.e. garnet plotting below the garnet lherzolite field of Sobolev et al. (1973; see also Sobolev 1977), was found. This garnet shows an X_{Mg} of 0.88, X_{Cr} of 0.21 and X_{Ca} of 0.11.

The compositions of orthopyroxenes are similar to those of the CE xenoliths with $En_{91.5–93.7}$ (Table 4). Orthopyroxenes from six of the fourteen xenoliths show distinct variations of Al and Cr with increasing contents

Table 4 Representative microprobe analyses of orthopyroxenes (wt%; *c* = core, *r* = rim). Legend of the samples see Table 2

	KGG31 Opx c	KGG16 Opx c	KGG63 Opx c	KGG63 Opx r	KGG13 Opx c	KGG45 Opx c	KGG23 Opx c	KGG20B Opx1 c	KGG20B Opx2 c	KGG14 Opx c	KGG62 Opx c
SiO_2	57.89	58.58	57.67	58.11	57.17	56.76	58.06	57.05	58.40	57.58	57.39
TiO_2	0.12	0.10	0.14	0.11	0.05	0.14	0.07	0.11	0.07	0.12	0.14
Al_2O_3	1.27	1.33	0.90	1.03	1.01	1.01	1.01	1.12	0.87	0.82	0.89
Cr_2O_3	0.49	0.33	0.21	0.24	0.34	0.28	0.43	0.18	0.21	0.20	0.33
MgO	34.26	34.29	34.36	35.10	35.30	34.86	35.31	34.89	34.95	35.05	34.66
CaO	0.73	0.81	0.43	0.47	0.61	0.58	0.55	0.69	0.50	0.38	0.40
MnO	0.12	0.13	0.12	0.09	0.11	0.07	0.16	0.13	0.13	0.15	0.11
FeO	5.13	5.47	5.35	5.29	4.93	5.28	5.06	5.42	5.90	5.32	5.51
Na_2O	0.15	0.12	0.11	0.15	0.13	0.11	0.11	0.12	0.10	0.08	0.11
K_2O	0.00	0.00	0.00	0.00	0.01	0.00	0.00	0.02	0.00	0.00	0.00
Total:	100.15	101.36	99.30	100.57	99.66	99.08	100.75	99.73	101.14	99.70	99.54
	KGG30 Opx c	KGG66 Opx c	KGG54 Opx c	KGG06 Opx c	KGG20A Opx c	KGG50 Opx c	KGG70 Opx c	KGG70 Opx r	KGG81 Opx c	KGG48 Opx c	KGG72 Opx1 c
SiO_2	57.85	57.88	58.19	57.80	58.81	57.82	58.81	58.23	58.40	57.72	57.93
TiO_2	0.12	0.09	0.13	0.14	0.06	0.07	0.09	0.15	0.09	0.05	0.05
Al_2O_3	0.83	0.96	1.13	0.90	1.12	0.93	0.88	1.11	0.96	1.46	1.00
Cr_2O_3	0.19	0.25	0.25	0.29	0.29	0.37	0.25	0.30	0.37	0.52	0.39
MgO	35.18	34.10	34.72	34.87	35.61	34.54	35.05	34.88	35.00	33.93	35.30
CaO	0.42	0.50	0.58	0.41	0.56	0.45	0.36	0.51	0.42	1.14	0.52
MnO	0.13	0.09	0.09	0.09	0.14	0.12	0.11	0.11	0.13	0.14	0.10
FeO	5.33	5.40	5.62	5.32	5.27	5.31	5.24	5.26	5.17	4.97	5.35
Na_2O	0.10	0.13	0.14	0.10	0.11	0.10	0.12	0.15	0.11	0.18	0.10
K_2O	0.01	0.01	0.00	0.00	0.00	0.02	0.00	0.02	0.00	0.03	0.00
Total:	100.15	99.40	100.85	99.93	101.97	99.72	100.90	100.71	100.65	100.14	100.74
	KGG72 Opx2 c	KGG72 Opx3 c	KGG62A Opx c	KGG83 Opx c	KGG77 Opx c	KGG55 Opx c	KGG71 Opx1 r	KGG71 Opx2 r	KGG60 Opx c	KGG36 Opx c	KGG65 Opx c
SiO_2	57.36	57.07	57.13	57.20	58.48	57.40	58.20	57.32	56.18	56.57	56.92
TiO_2	0.07	0.08	0.10	0.10	0.03	0.08	0.31	0.26	0.13	0.06	0.10
Al_2O_3	1.05	1.93	1.35	0.90	1.28	1.30	1.70	1.62	1.10	1.52	0.96
Cr_2O_3	0.44	0.39	0.49	0.38	0.47	0.99	0.68	0.65	0.23	0.49	0.40
MgO	34.93	34.96	34.53	35.23	34.50	34.59	34.44	34.83	34.87	33.62	35.17
CaO	0.61	0.44	0.82	0.46	0.80	0.81	1.14	0.88	0.59	1.06	0.44
MnO	0.12	0.18	0.13	0.10	0.15	0.10	0.08	0.06	0.11	0.14	0.05
FeO	5.50	5.29	4.73	4.73	5.58	5.35	4.49	4.46	5.37	5.36	4.92
Na_2O	0.09	0.14	0.17	0.13	0.13	0.17	0.19	0.18	0.16	0.16	0.13
K_2O	0.00	0.01	0.00	0.00	0.01	0.02	0.01	0.00	0.00	0.01	0.00
Total:	100.18	99.48	99.46	99.23	101.43	100.09	101.23	100.25	98.73	98.99	99.09
	KGG88A Opx c	KGG69 Opx r	KGG56 Opx r	KGG44A Opx r	KGG65A Opx c	KGG68 Opx c	KGG37 Opx c	KGG46 Opx r	KGG51 Opx c	KGG52 Opx r	KGG84 Opx c
SiO_2	58.11	56.64	56.60	57.53	56.94	57.80	57.11	58.25	57.67	56.70	57.82
TiO_2	0.12	0.10	0.39	0.05	0.29	0.07	0.11	0.05	0.07	0.19	0.00
Al_2O_3	0.86	1.80	1.54	1.72	1.67	1.26	1.29	1.64	1.60	1.68	1.60
Cr_2O_3	0.33	0.55	0.60	0.40	0.70	0.57	0.55	0.43	0.58	0.70	0.90
MgO	35.22	34.05	34.59	34.33	34.43	34.75	35.46	34.89	35.17	34.32	35.26
CaO	0.46	1.18	1.08	1.20	1.09	0.92	0.75	1.09	1.06	1.10	0.70
MnO	0.13	0.013	0.09	0.10	0.10	0.10	0.10	0.13	0.12	0.10	0.08
FeO	5.12	4.69	4.98	4.40	4.32	4.97	4.82	4.36	4.49	4.36	4.39
Na_2O	0.16	0.19	0.16	0.21	0.18	0.11	0.15	0.14	0.15	0.18	0.10
K_2O	0.00	0.00	0.03	0.00	0.01	0.01	0.04	0.00	0.00	0.01	0.00
Total:	100.51	99.32	100.06	100.94	99.74	100.54	100.35	100.98	100.91	99.34	100.84

of both elements from core to rim in two samples (e.g. sample KGG70 in Table 4) and a variability of Al and Ca in the other four xenoliths in separate domains.

Most clinopyroxenes are similar in composition and zonation pattern to those from the CE xenoliths (see samples KGG30, KGG37 and KGG50 in Table 5). The most strongly deformed xenoliths (KGG36, KGG48, KGG65A, KGG68 and KGG77), however, have clinopyroxenes with distinctly lower Na and higher Ca contents and commonly lack zoning and melt inclusions.

The olivines of the porphyroclastic xenoliths are similar to those from the coarse equant samples with $Fo_{90.5–92.8}$ (Fig. 3). In contrast to the olivines from the coarse equant xenoliths, Ca increases from core to rim in

Table 5 Representative microprobe analyses of clinopyroxenes (wt%; *c* = core, *r* = rim). Legend of the samples see Table 2

	KGG31 Cpx c	KGG16 Cpx c	KGG63 Cpx c	KGG13 Cpx c	KGG45 Cpx c	KGG23 Cpx c	KGG20B Cpx c	KGG14 Cpx c	KGG62 Cpx c	KGG30 Cpx c
SiO_2	54.11	55.46	53.78	55.21	55.08	55.17	55.56	54.96	53.95	54.89
TiO_2	0.19	0.12	0.43	0.10	0.33	0.17	0.08	0.24	0.37	0.24
Al_2O_3	2.55	2.66	3.09	2.12	2.75	2.14	2.22	2.84	2.54	2.66
Cr_2O_3	2.19	1.45	1.36	1.62	1.51	2.11	1.30	1.39	2.38	1.36
MgO	16.50	17.31	16.08	16.64	16.27	16.41	16.79	16.39	15.71	16.14
CaO	19.38	19.87	19.40	20.14	19.36	20.13	20.71	19.58	19.31	20.21
MnO	0.12	0.08	0.07	0.07	0.10	0.14	0.06	0.05	0.08	0.07
FeO	2.53	2.73	2.78	2.35	2.62	2.50	2.61	2.69	2.63	2.65
Na_2O	1.93	1.53	2.17	1.62	1.91	1.81	1.51	2.04	2.26	1.98
K_2O	0.02	0.05	0.00	0.00	0.00	0.03	0.03	0.02	0.00	0.04
Total:	99.51	101.24	99.15	99.87	99.92	100.60	100.86	100.19	99.23	100.23
	KGG30 Cpx r	KGG66 Cpx c	KGG54 Cpx c	KGG06 Cpx c	KGG20A Cpx c	KGG50 Cpx c	KGG70 Cpx c	KGG81 Cpx c	KGG48 Cpx c	KGG72 Cpx c
SiO_2	53.85	53.63	54.42	54.74	53.97	54.57	55.14	54.15	54.50	54.10
TiO_2	0.37	0.21	0.30	0.35	0.10	0.13	0.29	0.16	0.15	0.15
Al_2O_3	1.98	2.39	3.02	2.97	2.59	2.30	2.72	1.39	2.24	2.19
Cr_2O_3	1.41	1.16	1.45	1.86	1.32	1.78	1.68	2.50	1.32	1.84
MgO	16.40	16.64	16.48	16.08	16.98	16.47	16.25	16.58	18.57	16.59
CaO	23.06	20.87	19.60	19.69	19.58	19.78	19.63	20.99	19.16	19.58
MnO	0.02	0.04	0.09	0.07	0.06	0.04	0.08	0.11	0.08	0.14
FeO	2.46	2.40	2.74	2.58	2.51	2.50	2.42	2.37	2.88	2.63
Na_2O	0.93	1.39	2.02	2.26	1.77	1.78	2.14	1.36	1.17	1.79
K_2O	0.00	0.01	0.02	0.02	0.02	0.00	0.04	0.01	0.05	0.00
Total:	100.48	98.74	100.13	100.63	98.90	99.34	100.40	99.63	100.13	99.00
	KGG72 Cpx r	KGG62A Cpx c	KGG83 Cpx c	KGG77 Cpx c	KGG55 Cpx c	KGG55 Cpx r	KGG71 Cpx c	KGG60 Cpx c	KGG36 Cpx c	KGG65 Cpx c
SiO_2	52.91	54.75	55.74	55.40	54.54	54.18	54.11	54.48	54.82	54.02
TiO_2	0.21	0.23	0.15	0.07	0.19	0.22	0.52	0.33	0.10	0.23
Al_2O_3	1.95	2.36	2.15	2.23	2.49	0.25	2.62	2.89	2.41	2.63
Cr_2O_3	2.08	2.03	1.95	1.65	1.19	1.32	1.85	1.39	1.23	2.39
MgO	16.44	17.38	16.98	17.47	17.03	16.68	17.99	16.34	18.29	15.91
CaO	21.49	19.38	20.04	20.11	19.80	23.89	18.15	19.62	19.27	19.05
MnO	0.09	0.10	0.09	0.09	0.05	0.05	0.11	0.08	0.09	0.12
FeO	2.50	2.72	2.23	2.83	2.81	1.84	2.53	2.73	2.91	2.44
Na_2O	1.23	1.66	1.75	1.43	1.64	1.05	1.55	2.13	1.27	2.14
K_2O	0.01	0.03	0.01	0.00	0.02	0.03	0.02	0.00	0.05	0.00
Total:	98.91	100.65	101.08	101.27	99.75	99.50	99.45	99.99	100.45	98.92
	KGG88A Cpx c	KGG88A Cpx r	KGG69 Cpx c	KGG69 Cpx r	KGG56 Cpx c	KGG44A Cpx c	KGG65A Cpx c	KGG68 Cpx c	KGG37 Cpx c	KGG37 Cpx r
SiO_2	54.65	54.19	53.60	53.66	54.04	54.87	54.70	54.69	54.68	54.28
TiO_2	0.23	0.27	0.15	0.13	0.64	0.18	0.60	0.12	0.19	0.23
Al_2O_3	2.66	1.64	2.72	1.16	2.22	2.73	2.60	1.64	2.32	1.29
Cr_2O_3	2.30	2.68	1.49	1.51	1.80	1.13	1.80	1.27	1.95	2.66
MgO	15.59	16.16	18.74	17.86	17.99	18.34	17.82	18.51	17.34	17.27
CaO	19.40	20.70	17.87	21.18	18.84	18.57	18.43	20.38	19.22	21.77
MnO	0.10	0.10	0.09	0.12	0.08	0.09	0.11	0.09	0.05	0.12
FeO	2.27	2.34	2.85	2.48	2.30	2.92	2.50	2.54	2.30	2.24
Na_2O	2.30	1.47	1.36	0.97	1.37	1.40	1.54	0.91	1.61	1.02
K_2O	0.04	0.03	0.04	0.02	0.02	0.02	0.02	0.02	0.03	0.02
Total:	99.52	99.58	98.91	99.10	99.30	100.24	100.12	100.20	99.69	100.89

three samples (KGG16, KGG55, KGG70; see Table 6 and Figs. 5 and 6). Particularly high Ca contents are present in the rims adjacent to clinopyroxenes and to the kelyphitic rims of the garnets. In one sample (KGG70; cp. Table 7 and Fig. 5), olivine neoblasts have twice the amount of Ca relative to the core of the porphyroclasts.

Mosaic-porphyroclastic xenoliths (MP)

Six xenoliths classified as mosaic-porphyroclastic and laminated-mosaic-porphyroclastic after Harte (1977) show intensive dynamic recrystallisation of more than 90% of the olivine and partly of orthopyroxene. All

Table 6 Representative microprobe analyses of olivines (wt%; *c* = core, *r* = rim). Legend of the samples see Table 2

	KGG31 Ol c	KGG16 Ol c	KGG63 Ol c	KGG13 Ol c	KGG45 Ol c	KGG23 Ol c	KGG20B Ol c	KGG14 Ol c	KGG62 Ol c	KGG30 Ol c
SiO_2	41.29	41.27	40.93	40.68	42.01	41.67	41.53	40.96	41.48	40.72
TiO_2	0.00	0.01	0.03	0.07	0.03	0.02	0.00	0.00	0.01	0.02
Al_2O_3	0.03	0.04	0.00	0.00	0.03	0.02	0.01	0.00	0.00	0.00
Cr_2O_3	0.04	0.04	0.03	0.05	0.01	0.05	0.01	0.00	0.03	0.04
MgO	49.28	49.92	49.34	50.18	49.85	50.21	49.66	49.46	49.67	48.43
CaO	0.06	0.05	0.02	0.02	0.04	0.03	0.01	0.07	0.04	0.07
MnO	0.10	0.11	0.11	0.12	0.11	0.11	0.09	0.10	0.10	0.12
FeO	8.77	8.45	8.96	8.48	8.89	8.23	8.90	8.88	8.39	8.82
NiO	0.36	0.40	0.33	0.45	0.42	0.33	0.39	0.49	0.43	0.49
Total:	99.92	100.28	99.77	100.06	101.37	100.67	100.59	99.95	100.14	98.72
	KGG66 Ol c	KGG54 Ol c	KGG06 Ol c	KGG20A Ol c	KGG50 Ol1 c	KGG50 Ol2 c	KGG50 Ol3 c	KGG70 Ol c	KGG81 Ol c	KGG48 Ol c
SiO_2	40.44	41.04	40.88	41.07	41.81	41.81	41.33	40.68	41.06	41.27
TiO_2	0.02	0.00	0.02	0.00	0.00	0.00	0.01	0.00	0.03	0.05
Al_2O_3	0.00	0.00	0.05	0.02	0.00	0.04	0.00	0.00	0.01	0.03
Cr_2O_3	0.05	0.03	0.02	0.04	0.06	0.02	0.03	0.01	0.06	0.07
MgO	49.48	49.46	50.28	50.13	50.34	49.20	50.49	50.35	49.53	50.21
CaO	0.04	0.03	0.02	0.06	0.03	0.10	0.06	0.05	0.04	0.09
MnO	0.15	0.09	0.14	0.06	0.11	0.11	0.07	0.11	0.15	0.14
FeO	8.94	9.08	8.66	8.41	8.43	8.62	8.11	8.84	8.36	8.37
NiO	0.44	0.40	0.39	0.39	0.32	0.43	0.38	0.43	0.43	0.43
Total:	99.55	100.13	100.45	100.18	101.10	100.31	100.48	100.47	99.67	100.66
	KGG72 Ol c	KGG62A Ol c	KGG83 Ol c	KGG77 Ol c	KGG55 Ol c	KGG71 Ol r	KGG60 Ol c	KGG36 Ol c	KGG65 Ol c	KGG88A Ol c
SiO_2	41.08	41.85	42.40	41.36	40.96	42.28	40.84	41.04	41.04	41.54
TiO_2	0.00	0.03	0.02	0.00	0.01	0.01	0.06	0.01	0.04	0.02
Al_2O_3	0.01	0.05	0.01	0.03	0.04	0.04	0.01	0.00	0.01	0.02
Cr_2O_3	0.00	0.05	0.06	0.05	0.00	0.09	0.00	0.06	0.02	0.03
MgO	50.28	50.14	50.25	50.01	49.68	50.22	49.19	49.06	50.57	49.63
CaO	0.03	0.05	0.04	0.08	0.03	0.09	0.04	0.10	0.03	0.03
MnO	0.11	0.10	0.08	0.12	0.11	0.10	0.08	0.10	0.09	0.08
FeO	8.64	7.96	8.14	8.54	9.07	7.46	8.75	8.87	7.52	8.12
NiO	0.35	0.26	0.46	0.38	0.36	0.31	0.26	0.33	0.38	0.37
Total:	100.49	100.49	101.44	100.56	100.27	100.60	99.22	99.56	99.69	99.84
	KGG69 Ol r	KGG56 Ol r	KGG44A Ol r	KGG65A Ol c	KGG68 Ol c	KGG37 Ol c	KGG46 Ol r	KGG51 Ol c	KGG52 Ol r	KGG84 Ol c
SiO_2	41.73	41.65	41.34	41.77	41.17	40.64	41.11	41.36	40.80	41.78
TiO_2	0.00	0.03	0.01	0.03	0.01	0.00	0.00	0.00	0.04	0.00
Al_2O_3	0.03	0.02	0.04	0.06	0.00	0.02	0.00	0.00	0.05	0.07
Cr_2O_3	0.09	0.03	0.04	0.05	0.03	0.05	0.03	0.07	0.09	0.11
MgO	50.31	50.78	48.92	50.35	50.00	50.16	50.96	51.05	50.85	50.62
CaO	0.06	0.07	0.08	0.10	0.11	0.06	0.08	0.08	0.06	0.05
MnO	0.10	0.08	0.07	0.10	0.12	0.09	0.14	0.11	0.12	0.13
FeO	8.06	7.58	8.98	7.51	8.21	7.77	7.61	7.15	7.55	6.98
NiO	0.40	0.45	0.39	0.46	0.26	0.35	0.36	0.39	0.41	0.44
Total:	100.77	100.67	99.86	100.42	99.92	99.12	100.28	100.21	99.95	100.17

samples are garnet harzburgites and display a mylonitic foliation with an elongation of garnet and orthopyroxene into the foliation (see Fig. 4d).

The homogeneous garnets of the mosaic-porphyroclastic xenoliths generally with diameters less than 3 mm reveal X_{Mg}-values of 0.84–0.87, X_{Cr} of 0.07–0.21 and X_{Ca} of 0.12–0.21 (Table 3). A weak increase of pyrope and a decrease of Cr from core to rim is eventually observed. Overall, these garnets have the highest Mg and Cr contents of all xenoliths investigated.

Orthopyroxenes and olivines have high X_{Mg}-values ($En_{91.4–93.7}$ and $Fo_{90.9–92.6}$, respectively.). Orthopyroxenes yield distinctly higher Al and Ca contents than those from the coarse equant and the porphyroclastic xenoliths, and olivines have the highest Ca contents. No systematic zonation patterns are observed either in porphyroclasts or neoblasts. The Ca contents in orthopyroxenes in two samples (e.g. KGG71 in Table 4) differ slightly from grain to grain.

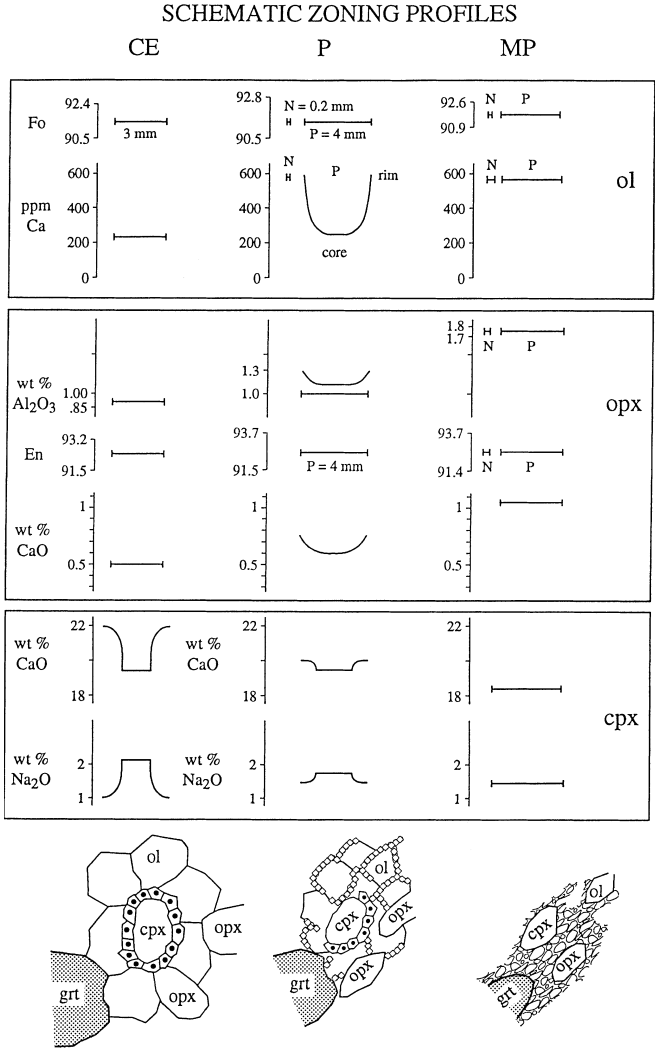

Fig. 5 Schematic zoning profiles of olivine, orthopyroxene and clinopyroxene in coarse equant, porphyroclastic and mosaic-porphyroclastic xenoliths; (*N* neoblasts, *P* porphyroclasts)

The compositions of clinopyroxenes are similar to those of the most strongly deformed P xenoliths (Table 5). In only one sample (see KGG69 in Table 5) is a thin rim present depleted in Na and enriched in Ca. Melt inclusions were not observed.

Thermobarometry

Pressures and temperatures of crystallisation of peridotites have been estimated with the following geothermobarometers in eight combinations:

T BKN = Two pyroxene geothermometer of Brey and Köhler (1990)
T Ca-opx = Ca-in-opx thermometer of Brey and Köhler (1990)
T Na-px = Empirical Na opx-cpx thermometer of Brey and Köhler (1990)
T KRO = Grt-cpx Fe-Mg thermometer of Krogh (1989)
T ONW = Grt-ol Fe-Mg thermometer of O'Neill and Wood (1979, 1981)

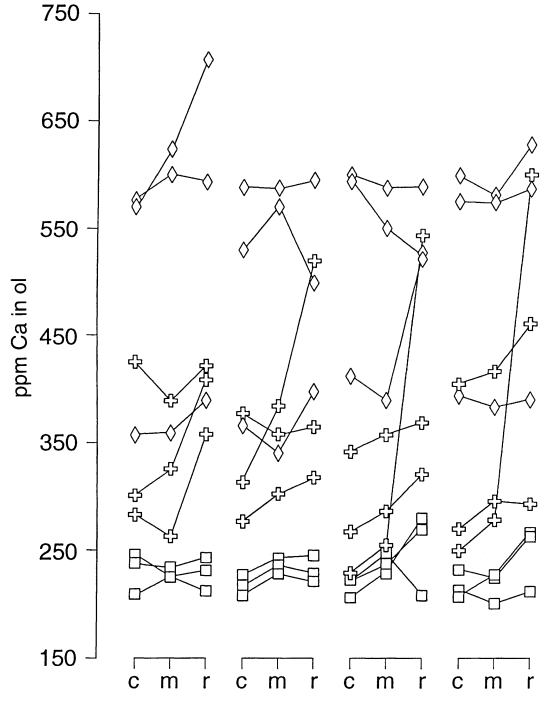

Fig. 6 Ca contents of olivines from coarse equant (*squares*), porphyroclastic (*crosses*) and mosaic-porphyroclastic xenoliths (*diamonds*); *c* core, *m* intermediate, *r* rim)

T HA = Grt-opx Fe-Mg thermometer of Harley (1984)
P BKN = Al-in-opx barometer of Brey and Köhler (1990)
P Cr = Cr-in-opx barometer of Nickel (1989)
P KB = Ca-in-ol barometer of Köhler and Brey (1990)

All thermometers were combined with the barometer *P* BKN and in addition the two pyroxene thermometer *T* BKN with the barometers *P* KB and *P* Cr. All eight applied combinations should yield similar results within their respective error limits if the minerals were in thermodynamic equilibrium and other chemical parameters such as Fe^{3+} were negligible. Compared to the potentially most accurate combination *T* BKN + *P* BKN we found both agreement and disagreement with the various thermobarometers. The comparisons are shown in detail in Figs. 7 and 8. Figure 7 shows the outcome of *P*-*T* estimates with the combinations *T* BKN + *P* BKN, *T* Ca-opx + *P* BKN, and *T* BKN + *P* KB for one xenolith each of the coarse equant, the porphyroclastic and the mosaic-porphyroclastic type:

Sample KGG72 is a coarse equant xenolith without any visible dynamic recrystallisation and with only minor cataclastic fracturing. The combination *T* BKN + *P* BKN gives on average about 37.5 kbar and 1080°C when core compositions of orthopyroxene and clinopyroxene are combined (Fig. 7a). Somewhat lower temperatures are obtained, when compositions towards the rims of orthopyroxene and clinopyroxene are combined. This is entirely due to a slight zonation in clinopyroxene while the Al content of orthopyroxene remains constant from core to rim. Thus, lower temperatures and, consequently, lower pressures are calculated.

Table 7 Ca content (ppm) of olivines from selected samples; (*c* = core, *m* = intermediate, *r* = rim)

Coarse equant xenoliths:												
KGG13:	Ol 1	Ol 1	Ol 1	Ol 2	Ol 2	Ol 2	Ol 3	Ol 3	Ol 3	Ol 4	Ol 4	Ol 4
	c	m	r	c	m	r	c	m	r	c	m	r
	238	233	241	213	240	243	218	233	266	227	221	256
KGG63:	Ol 1	Ol 1	Ol 1	Ol 2	Ol 2	Ol 2	Ol 3	Ol 3	Ol 3	Ol 4	Ol 4	Ol 4
	c	m	r	c	m	r	c	m	r	c	m	r
	208	224	211	207	228	227	203	226	274	208	197	207
KGG72:	Ol 1	Ol 1	Ol 1	Ol 2	Ol 2	Ol 2	Ol 3	Ol 3	Ol 3	Ol 4	Ol 4	Ol 4
	c	m	r	c	m	r	c	m	r	c	m	r
	244	233	230	225	229	220	218	243	204	203	219	259
Porphyroclastic xenoliths:												
KGG16:	Ol 1	Ol 1	Ol 1	Ol 2	Ol 2	Ol 2	Ol 3	Ol 3	Ol 3	Ol 4	Ol 4	Ol 4
	c	m	r	c	m	r	c	m	r	c	m	r
	427	392	417	366	358	364	340	356	365	398	413	457
KGG55:	Ol 1	Ol 1	Ol 1	Ol 2	Ol 2	Ol 2	Ol 3	Ol 3	Ol 3	Ol 4	Ol 4	Ol 4
	c	m	r	c	m	r	c	m	r	c	m	r
	283	263	357	275	301	318	268	285	317	267	283	288
KGG70:	Ol 1	Ol 1	Ol 1	Ol 2	Ol 2	Ol 2	Ol 3	Ol 3	Ol 3	Ol 4	Ol 4	Ol 4
	c	m	r	c	m	r	c	m	r	c	m	r
	302	324	412	312	382	517	229	249	540	249	279	594
Mosaic-porphyroclastic xenoliths:												
KGG56:	Ol 1	Ol 1	Ol 1	Ol 2	Ol 2	Ol 2	Ol 3	Ol 3	Ol 3	Ol 4	Ol 4	Ol 4
	c	m	r	c	m	r	c	m	r	c	m	r
	357	357	387	365	338	394	409	389	525	389	379	385
KGG69:	Ol 1	Ol 1	Ol 1	Ol 2	Ol 2	Ol 2	Ol 3	Ol 3	Ol 3	Ol 4	Ol 4	Ol 4
	c	m	r	c	m	r	c	m	r	c	m	r
	570	623	706	588	595	598	587	588	588	572	572	584
KGG71:	Ol 1	Ol 1	Ol 1	Ol 2	Ol 2	Ol 2	Ol 3	Ol 3	Ol 3	Ol 4	Ol 4	Ol 4
	c	m	r	c	m	r	c	m	r	c	m	r
	575	601	594	528	570	497	595	549	524	598	578	626

However, clinopyroxene rims are apparently not in equilibrium with orthopyroxene rims or cores anymore. It rather seems, that the composition of clinopyroxene is influenced by melting processes, which led to the formation of their serrated rims. These rims were apparently not formed in equilibrium with orthopyroxene, because they are richer (compared to cpx cores) in CaO, TiO_2 and depleted in Na_2O and Al_2O_3 with no concommitant changes in orthopyroxene. The apparently low temperatures and pressures shown in Fig. 7a for the formation of the serrated rims are unrealistic. The *P-T* conditions obtained with *T* Ca-opx + *P* BKN scatter at around 36.5 kbar and 1000°C (Fig. 7a) for both rim and core compositions. These conditions are on average lower than those calculated with *T* BKN + *P* BKN for core composition but marginally overlap. The two thermometers are in better agreement in other samples, but disagreement outside the mutual errors of the methods also occurs (see below). There is good agreement for combinations of core compositions with *T* BKN + *P* KB and *T* BKN + *P* BKN and similarly for intermediate and rim compositions. As for *T* BKN + *P* BKN this range in calculated *P* and *T* is entirely due to the zonation in clinopyroxene whereas the composition of olivine varies only little (see Fig. 6). The formation of the serrated rims of the clinopyroxenes must be due to melting processes, which affected only clinopyroxene.

Sample KGG70 (Fig. 7b) is a porphyroclastic xenolith with only about 2% recrystallized olivine neoblasts. Clinopyroxenes in this sample are constant in composition whereas Al in orthopyroxene slightly increases from core to rim. Consequently, an apparent range of pressures from about 40 kbar (rim) to 46 kbar (core) is obtained, seemingly reflecting an upheavel of a portion of the earth's mantle at constant temperature. An alternative explanation would be a shortlived heating event to a maximum possible temperature of about 1150°C (see arrow in Fig. 7b) associated with deformation to which only orthopyroxene and olivine partly adjusted in composition, but not clinopyroxene. A thermal overprint is also indicated by the very high (at the rims) and highly variable Ca contents in olivine (Fig. 6) which leads to extremely low calculated pressures with *T* BKN + *P* KB for rim compositions and combinations with olivine neoblasts.

Sample KGG71 (Fig. 7c) is a strongly deformed, mosaic-porphyroclastic xenolith with more than 90% of the olivine recrystallized. There is no zonation observed in the minerals and pressures and temperatures estimated with *T* BKN + *P* BKN and *T* BKN + *P* KB give a tight cluster at around 45 kbar and 1250°C. Conditions calculated with *T* Ca-opx overlap entirely for two grains but one orthopyroxene grain has a somewhat lower CaO content.

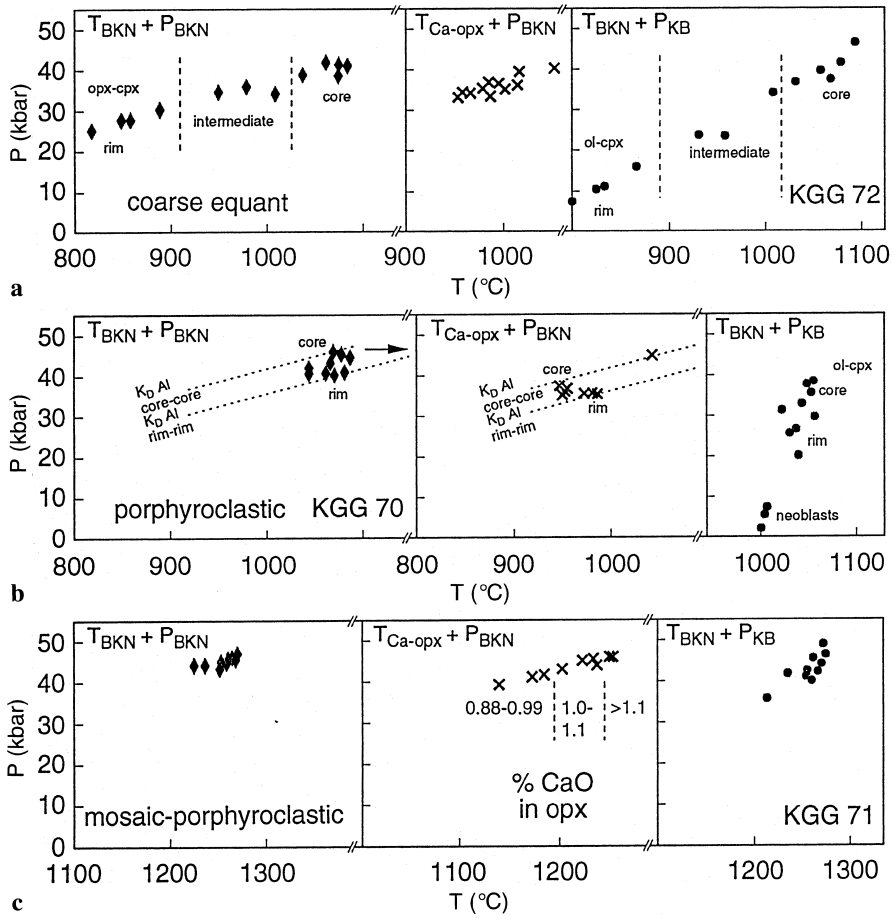

Fig. 7a–c Comparison of different combinations of geothermometers and -barometers for a coarse equant, a porphyroclastic and a mosaic-porphyroclastic xenolith

Estimation of pressures and temperatures of last equilibration

One set of mineral compositions considered to represent the stage of last equilibration was selected from each of the thirty-eight xenoliths to estimate pressures and temperatures with *T* BKN + *P* BKN (Fig. 8a) and *T* Ca-opx + *P* BKN (Fig. 8b) and for four harzburgites with *T* ONW + *P* BKN. These analyses were those from the cores of the minerals. Thus we estimate pressures and temperatures of crystallisation for the coarse equant xenoliths *before* the formation of the serrated rims of the clinopyroxenes, for the porphyroclastic samples *before* the onset of the plastic deformation and for the mosaic-porphyroclastic samples *during* plastic deformation. The combination *T* BKN + *P* BKN yields an alignment of the coarse equant xenoliths along a conductive continental geotherm of about 44 mW/m^2 with which two of the porphyroclastic xenoliths coincide (Fig. 8a). Other porphyroclastic xenoliths plot at higher temperatures at similar pressures and coincide with the highly deformed mosaic-porphyroclastic samples. Two mosaic-porphyroclastic samples plot at the highest pressures and temperatures and one of these is almost in the stability field of diamond.

The combination *T* Ca-opx + *P* BKN does not yield an alignment along a conductive continental geotherm. The coarse equant samples rather form a cluster between 35 and 41 kbar with a range in temperatures between 930 and 1100°C (Fig. 8b). The porphyroclastic and the mosaic-porphyroclastic xenoliths give similar pressures and temperatures as for the combination *T* BKN + *P* BKN. The reduction in the range of estimated pressures for the coarse equant samples is due to much lower temperatures calculated with *T* Ca-opx compared to *T* BKN and consequently lower calculated pressures. This indicates that some of the coarse equant peridotites were frozen in at a stage of cooling to which only Ca in opx adjusted.

Disequilibrium and cooling should be reflected by differences in calculated *P*,*T* conditions with other geothermobarometers. Figure 8c shows the temperature differences *T* Ca-opx - *T* BKN both calculated with *P* BKN plotted against the temperature from *T* BKN (+ *P* BKN). Brey (1990) deduced from a comparison with experiments in natural lherzolitic systems (Brey et al. 1990) that the 2 σ standard deviation of the temperature differences for these two thermometers is ±60°C. On this basis eight of the coarse equant and two porphyroclastic samples plot at too low temperatures and indicate dis-

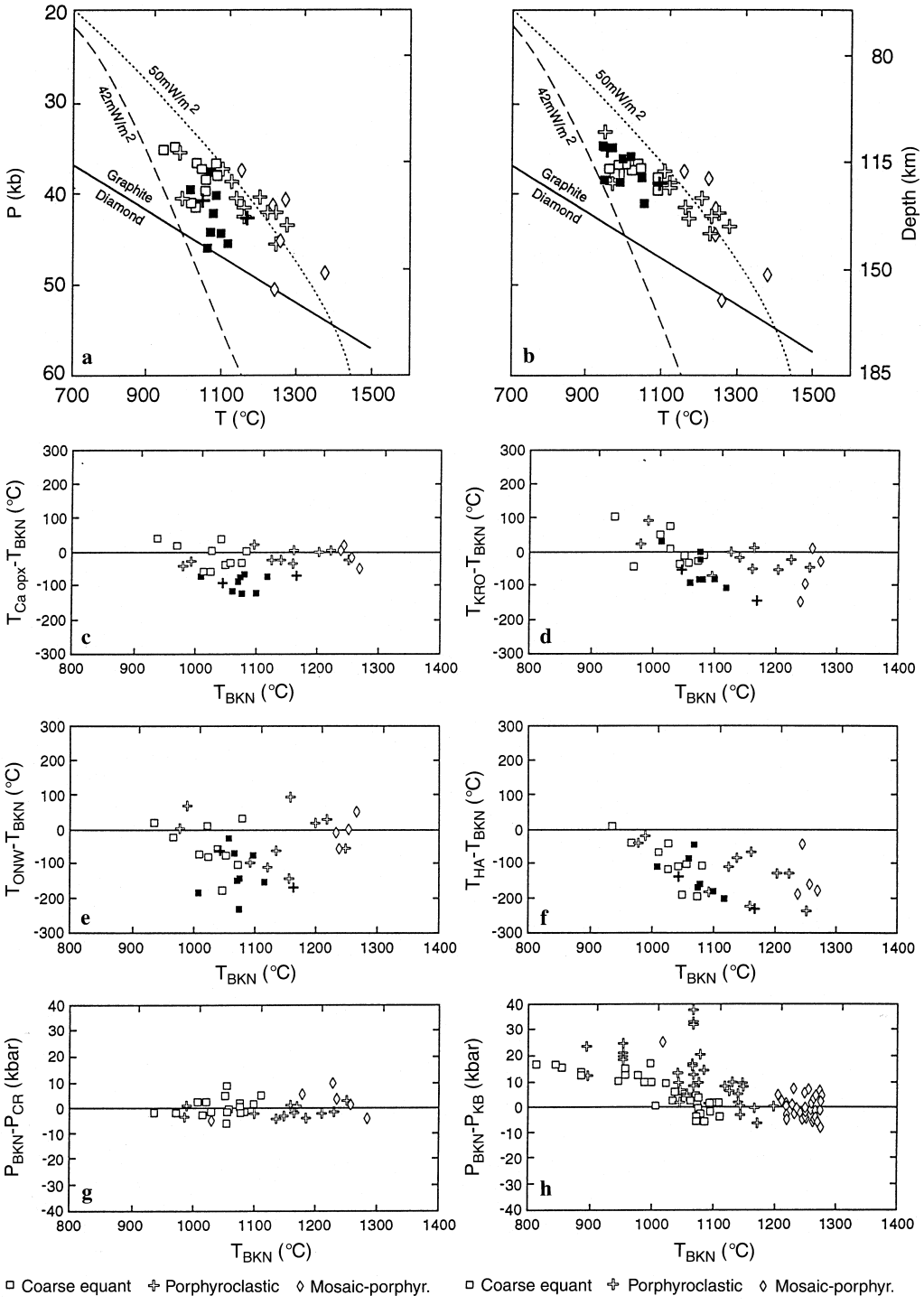

Fig. 8a–h Pressure-temperature estimates and comparisons with various combinations of thermometers and barometers for all samples investigated. Graphite-diamond transition after Kennedy and Kennedy (1976), geothermal gradients after Pollack and Chapman (1977). The significance of the data points in *solid ornament* is explained in the text. **a** *P-T* estimates with *T* BKN and *P* BKN (garnet lherzolites) and *T* ONW and *P* BKN (garnet harzburgites). b *P-T* estimates with *T* Ca-opx and *P* BKN (garnet lherzolites) and *T* ONW & *P* BKN (garnet harzburgites). **c** Diagram of *T* Ca-opx-*T* BKN against *T* BKN. **d** Diagram of *T* KRO-*T* BKN against *T* BKN. **e** Diagram of *T* ONW-*T* BKN against *T* BKN. **f** Diagram of *T* HA-*T* BKN against *T* BKN. **g** Diagram of *P* BKN-*P* Cr against *T* BKN. **h** Diagram of *P* BKN-*P* KB against *T* BKN

equilibrium between orthopyroxene and clinopyroxene. These samples are marked by filled symbols in Figs. 8 a–f, and should show deviations in similar directions for other combinations of geothermobarometers. Figures 8d–f show the comparison of three Fe-Mg exchange thermometers with the two pyroxene thermometer *T* BKN in diagrams similar to Fig. 8c. These thermometers with inherently larger uncertainties than *T* BKN

and T Ca-opx are further hampered by the assumption of all Fe being Fe^{2+}. The resultant 2 σ standard deviations for the comparison with the experiments are accordingly higher and are ± 100°C for T KRO - T BKN and ± 180°C for T ONW - T BKN (Brey 1990). The filled symbols plot consistently towards the lower end for negative temperature deviations though mostly within the 2 σ standard deviation range (Figs. 8 d,e). All samples plot to negative temperature deviations for the comparison T HA - T BKN and increasingly so with increasing T BKN. This reflects the systematic underestimation of temperatures with increasing temperature above 1000°C with the thermometer by Harley (1984) for peridotitic systems as shown by Brey and Köhler (1990). Nevertheless, the filled symbols tend to plot at the largest temperature deviations for each calculated T BKN.

The comparison of pressures calculated with P BKN and P Cr is very favourable and deviations are within ± 5 kbar (2 σ - see Fig. 8 g).

Indications for a thermal overprint

To further test for internal mineral equilibrium we compared pressures calculated with P KB + T BKN with P BKN + T BKN (Fig. 8 h) for the nine samples in which Ca was measured as a trace element in olivine (Fig. 6). Combinations of core compositions are in agreement in calculated pressures for all three textural types within the ± 7 kbar (2 σ) standard deviation derived by experiment (Brey 1990). Calculated pressure differences are up to + 40 kbar for combinations of rim compositions, indicating that the Ca contents in olivine rims are too high to be in equilibrium with the Al content in orthopyroxene. The high Ca contents are most likely due to a transient heating event, which is reflected only in olivine because of the high diffusion coefficient for Ca (see Jurewicz and Watson 1988 and for discussion Köhler et al. 1991).

Discussion and conclusions

a. Disequilibria in mantle xenoliths caused by thermal and deformational processes in the mantle

We find from thermobarometric calculations, that the upper mantle samples from Gibeon Townsland 1 were entrained in a kimberlite magma and erupted to the earth's surface from different states of physical conditions. Most of the coarse equant and the mosaic-porphyroclastic xenoliths reflect thermal equilibrium for the individual portions of the mantle from which they originate; other coarse equant xenoliths indicate a state of ongoing cooling while the porphyroclastic samples show a state of transient heating. This heating is expressed in an increase of Al and Ca in orthopyroxene and of Ca in olivine towards the rims. The composition of orthopyroxene indicates an increase of the temperature by about 30 °C and a drop in pressure (uprise) by 2–3 kbar (Fig. 7b). A few of the porphyroclastic and all mosaic-porphyroclastic xenoliths yield the highest temperatures of up to 1300 °C. As demonstrated above, this transient heating was coupled with intense deformation of the lower lithosphere. This is reminiscent of rift initiation by plastical stretching of the lithosphere as described by Nicolas et al. (1994), a process which is only possible when the mantle is warmed at least 150 °C above its initial temperature. Such locally elevated temperatures cannot be maintained over a longer period of time in the mantle. The absence of chemical zonation in the minerals of the mosaic-porphyroclastic xenoliths and thus of any sign of subsequent cooling indicates a rapid uplift of these rocks and a freezing of the equilibria by adiabatic cooling (see also Franz et al. 1996).

b. Characterization of the origin of the mantle xenoliths and inferences about the lithospheric development in Southern Africa

From geothermobarometry and the modal and mineral chemical composition we may deduce that the mantle underneath the Gibeon Kimberlite Province in the depth range of 100–140 km and at the time of the eruption of the kimberlites was at a thermal status corresponding to a geothermal gradient of about 44 mW/m^2 (see Figs. 8 and 9). It consisted of relatively fertile lherzolite intermingled with depleted harzburgitic material with temperatures up to 200°C higher than the lherzolites. Part of the lherzolitic material is also heated to similar temperatures. This may reflect local heating and deformation of a pre-existing chemically stratified mantle by intruded magma shortly before the eruption of the kimberlites. Because of the petrographic similarities (see Boyd and Mertzman 1987 and Fig. 10) we may suggest that the harzburgites are remnants of a cratonic mantle, and the Kaapvaal craton and its attached mantle may have extended formerly to the Gibeon Province (Hoal et al. 1995). A Re-Os model age of 2.1 Ga for a mosaic-porphyroclastic xenolith from the Gibeon Kimberlite Province (Pearson et al. 1994 and personal communication) does not refute this since a major assumption for these model ages is a single stage melting event whereby all the Re was driven off from the residue with the melt. Later refertilisation with reintroduction of Re results in younger model ages.

These findings may lead to the following geotectonic models:

1. The western border of the Kaapvaal craton and the depth to which it extends is not known with certainty (Hoal et al. 1995). It is also not known whether fragments of the Kaapvaal craton were involved in the tec-

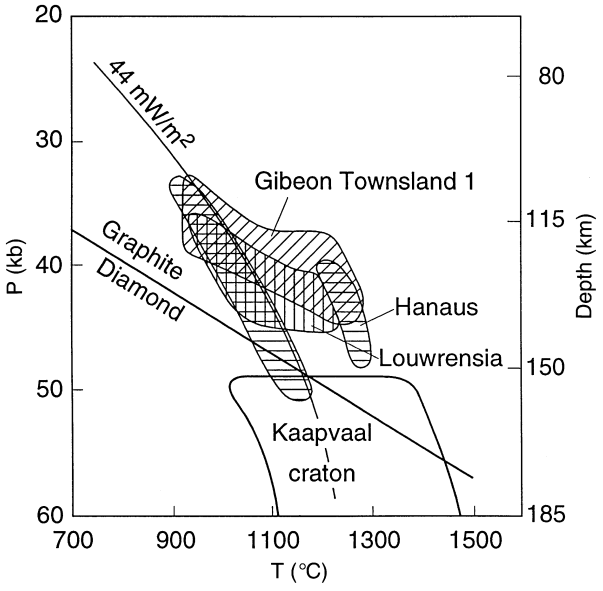

Fig. 9 Comparison of pressure temperature estimates with *T* BKN and *P* BKN for garnet peridotites (which give internally consistent *P-T* estimates also with all other combinations of geothermobarometers) from Gibeon Townsland 1 pipe (*vertical hatching* – data source this work), the Louwrensia pipe (*horizontal hatching*), the Hanaus pipe (*oblique hatching*) and from various localities from the Kaapvaal craton (data sources in Brey, 1990)

tonometamorphic evolution of the Rehoboth Subprovince (Hartnady et al. 1985). Thus it may well be possible that parts of old cratonic lithosphere are still present below Namibia, e.g. forming a wedge shaped continuation of the Kaapvaal craton towards the west or as small lithospheric slices. During hot spot activity and upwelling of asthenosphere, parts of this cratonic mantle could have been strongly deformed and finally erupted with the kimberlites.

2. Present models for the continental lithosphere of Southern Africa (Boyd and Gurney 1986; Haggerty 1994) indicate a distinct decrease in thickness from cratonic to off-craton areas, which results in compelling differences in thermal and geochemical properties of the mantle (see Fig. 9). Highly deformed mosaic-porphyroclastic peridotites with cratonic modal and chemical signatures in the xenolith suite of these off-craton kimberlites may be portions of tectonically transported subcratonic lower lithosphere caused by decoupling of lithosphere and underlying mantle (Wilson 1963). This process is influenced by the strong contrasts in viscosity between lithosphere and asthenosphere as pointed out by Sabadini et al. (1990, 1992). A tectonic transport of Kaapvaal lithosphere towards the Gibeon area could only take place if the African plate showed a relative motion towards the east or northeast. Such a motion is apparent from the relative motions of deeply rooted hot spots like Vema, Marion, Shona, Tristan or Bouvet (Duncan 1981; Hartnady and le Roex 1985; Spriggs

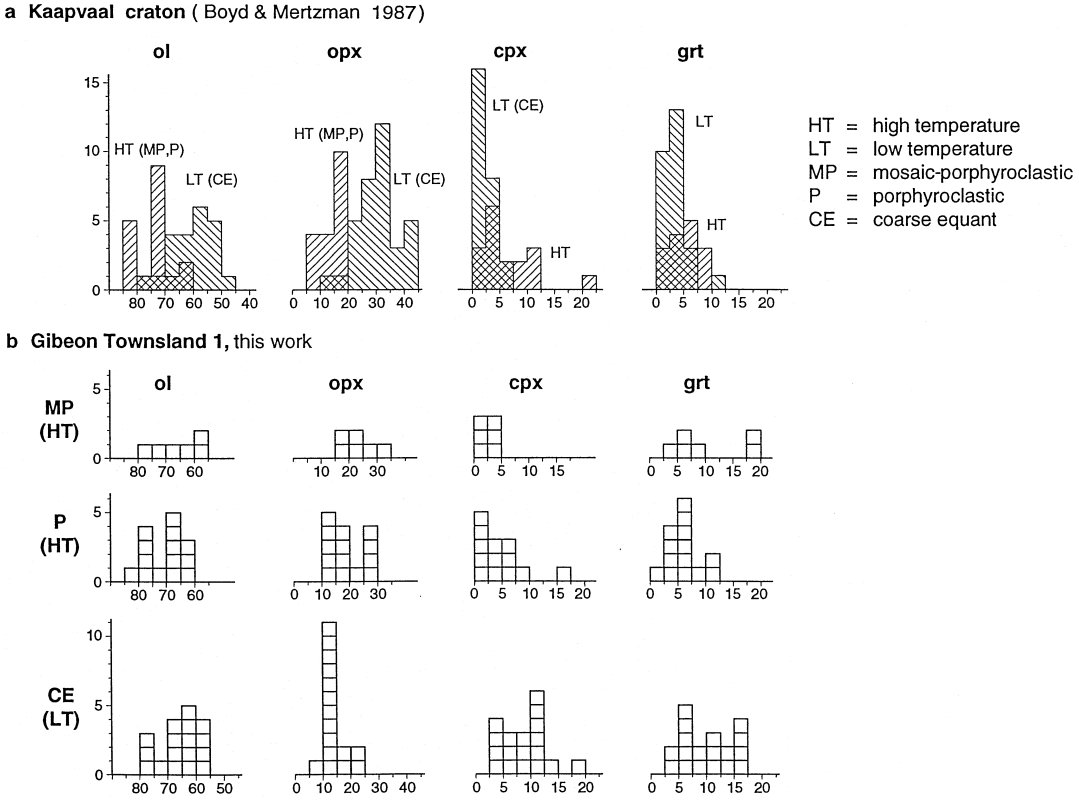

Fig. 10 Comparison of the modal mineral contents of garnet peridotites from the Kaapvaal craton and the Gibeon Townsland 1 pipe

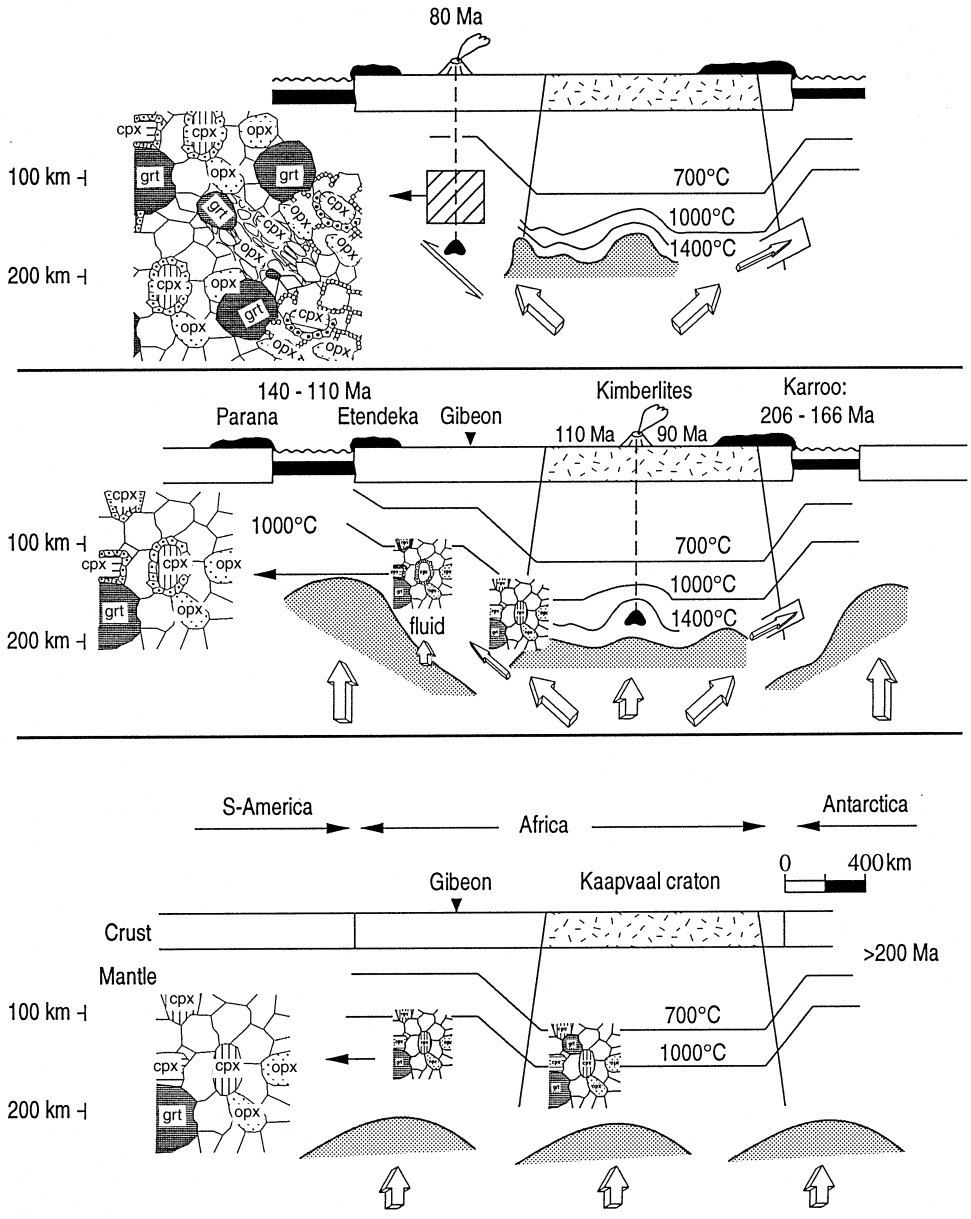

Fig. 11 Model for the evolution of crust and upper mantle beneath Southern Africa during the last 200 Ma

1988). These hot spots always show relative motions towards the southwest and thus indicate a drift of the African plate towards the northeast. These observations are in accordance with the unidirectional flow model of Pavoni (1993), which explains the extensional regime in the Mesozoic and Tertiary by the rise of warm asthenospheric material in the centre of the African continent. At the base of the lithosphere the upwelling mantle material is then diverging and radially flowing away from the centre. The major plate driving force is shear traction exerted by the convecting mantle at the base of the lithosphere. This way, parts of the lower Kaapvaal lithosphere may have been transported below Southern Namibia and later on sampled by the kimberlites on their way to the surface.

A possible scenario based on this model is schematically shown in the sequence of Fig. 11. The lowermost part of the cartoon shows the situation as it may have existed more than 200 Ma ago, when South America, Africa and Antarctica/Australia were still joined and shortly before the breakup of Gondwana. The mantle underneath the Kaapvaal craton was colder at any depth at least down to 200 km than in the adjoining younger(?) mantle underneath the younger crustal areas of Namibia. At about 190 Ma ago large mantle plumes (superplumes in the sense of Larson 1991 and Haggerty 1994) were rising upwards whose ascent was inhibited, delayed and deflected by the cold, rheologically strong mantle underneath the craton (Fig. 11, middle part), which is in accordance with thermomechanical modelling of Nico-

las et al. (1994). Material flowing around this cold block led to the breakup of Gondwana and to the the eruption of the Karroo basalts (190 Ma) and the Parana and Etendeka flood basalts (140–120 Ma). The impact of the plume onto the cold mantle may have led to partial breakup of the Kaapvaal mantle, to the introduction of metasomatizing fluids and to the generation of low melt fractions (kimberlites), which may eventually have erupted to the surface (120 and 90 Ma ago) and brought with them different kinds of mantle material and diamonds. The heat input and the tectonic activity caused by these plumes led to a detachment of slices of the lower cratonic lithosphere. Further movements of the plumes as well as the relative movement of the sublithospheric mantle towards the southwest induced the tectonic transport of delaminated Kaapvaal mantle slices underneath the Gibeon area. Such delaminations of subcontinental lithosphere and their transport towards the Atlantic ocean have already been postulated for the period of Etendeka and Parana volcanism by Hawkesworth et al. (1986). In the Gibeon Kimberlite Province the precursors of the mantle magmatism (Fig. 11, middle part) percolated through the older, pre-existing mantle and reacted with it to form the serrated clinopyroxene rims. Finally, the heat input and the fluid phase of the mantle plumes generated kimberlitic, olivine melilitic and carbonatitic melts in the Gibeon Kimberlite Province. At the base of the lithosphere plastic stretching and heat input induced the development of the mosaic-porphyroclastic textures and the complete thermal re-equilibration in the harzburgitic xenoliths. These deformed xenoliths as well as parts of the mantle underlying the Gibeon Kimberlite Province were transported together to the surface by the kimberlites of the Gibeon area about 80 Ma ago (Fig. 11, upper part).

Acknowledgements This research project was part of the "Gross Brukkaros-project" of the department of geosciences at the University of Würzburg. Funding of the University and of the Deutsche Forschungsgemeinschaft (DFG) and logistic support by the Geological Survey of Namibia are gratefully acknowledged. We thank C. Ruprecht, P. Richter and R. Baur for help with X-ray fluorescence analyses and the Namibia team of the University of Würzburg for lively discussions in the field and at home. We owe great thanks to S. Haggerty and an anonymous reviewer, who critically read an earlier version of the manuscript. We also would like to thank B. Dawson for the review of the final version of this paper.

References

Boyd FR, Gurney JJ (1986) Diamonds and the African lithosphere. Science 232: 472–477

Boyd FR, Mertzman SA (1987) Composition and structure of the Kaapvaal lithosphere, southern Africa. In: Mysen BO (ed) Magmatic processes: physicochemical principles. Geochem Soc Spec Publ, pp

Brey GP (1990) Geothermobarometry for lherzolites: experiments from 10 to 60 kbar, new thermobarometers and application to natural rocks. Habilitation thesis, Univ Darmstadt, Germany

Brey GP, Köhler T (1990) Geothermobarometry in four-phase lherzolites. II. New thermobarometers, and practical assessment of existing thermobarometers. J Petrol 31: 1353–1378

Brey GP, Köhler T, Nickel KG (1990) Geothermobarometry in four-phase lherzolites. I. Experimental results from 10 to 60 kbar. J Petrol 31: 1313–1352

Clement RC, Skinner EMW (1985) A textural-genetic classification of kimberlites. Trans Geol Soc S Afr 88: 403–409

Clifford TN (1966) Tectono-metallogenetic units and metallogenic provinces of Africa. Earth Planet Sci Lett 1: 421–434

Duncan RA (1981) Hotspots in the Southern Oceans – an absolute frame of reference for the motion of the Gondwana continents. Tectonophysics 74: 29–42

Franz L, Brey GP, Okrusch M (1996) Re-equilibration of ultramafic xenoliths from Namibia by metasomatic processes at the mantle boundary. J Geol 104: 599–615

Haggerty SE (1994) Superkimberlites: a geodynamic diamond window to the Earth's core. Earth Planet Sci Lett 122: 57–69

Harley SL (1984) An experimental study of the partitioning of Fe and Mg between garnet and orthopyroxene. Contrib Mineral Petrol 86: 359–379

Harte B (1977) Rock nomenclature with particular relation to deformation and recrystallisation textures in olivine-bearing xenoliths. J Geol 85: 279–288

Hartnady CJ, le Roex AP (1985) Southern ocean hotspot tracks and the Cenozoic absolute motions of the African, Antarctic and South American plates. Earth Planet Sci Lett 75: 245–257

Hartnady CJ, Joubert P, Stowe C (1985) Proterozoic crustal evolution in Southwestern Africa. Episodes 8: 236–244

Hawkesworth CJ, Mantovani MSM, Taylor PN, Palacz Z (1986) Evidence from the Parana of south Brazil for a continental contribution to Dupal basalts. Nature 322: 356–358

Hoal BG, Hoal KEO, Boyd FR, Pearson DG (1995) Tectonic setting and mantle composition inferred from peridotite xenoliths, Gibeon Kimberlite Field, Namibia(abstract). In: Sixth Int Kimberlite Conf, Novosibirsk, Extended Abstr 1, pp. 239–241

Janse AJA (1964) Kimberlites and related rocks of the Nama plateau SWA. PhD thesis, Univ Leeds, England

Janse AJA (1971) Monticellite bearing porphyritic peridotite from Gross Brukkaros SWA. Trans Geol Soc S Afr 74: 45–55

Janse AJA (1975) Kimberlite and related rocks from the Nama-Plateau of South-West Africa. Phys Chem Earth 9: 81–94

Jurewicz AJG, Watson EB (1988) Cations in olivine. 2. Diffusion in olivine xenocrysts with applications to petrology and mineral physics. Contrib Mineral Petrol 99: 186–201

Kennedy CS, Kennedy GC (1976) The equilibrium boundary between graphite and diamond. J Geophys Res 81: 2467–2470

Köhler T, Brey GP (1990) Calcium exchange between olivine and clinopyroxene calibrated as a geothermobarometer for natural peridotites from 2 to 60 kbar with applications. Geochim Cosmochim Acta 54: 2375–2388

Köhler T, Palme H, Brey GP (1991) Determination of meteorite cooling rates using calcium exchange between olivine and clinopyroxene. Neues Jahrb Mineral Monatsh 9: 423–431

Kretz R (1983) Symbols for rock-forming minerals. Am Mineral 68: 277–279

Krogh EJ (1988) The garnet-clinopyroxene Fe-Mg geothermometer – a reinterpretation of existing experimental data. Contrib Mineral Petrol 99: 44–48

Kurszlaukis S (1994) Geology and geochemistry of the carbonatitc Gross Brukkaros Volcanic Field and the ultrabasic Blue Hills Intrusive Complex, southern Namibia. PhD thesis, Univ Würzburg, Germany

Kurszlaukis S, Franz L, Brey GP (1995) Geochemistry and evolution of the ultrabasic Blue Hills Intrusive Complex (Namibia)(abstract). In: Sixth Int Kimberlite Conf, Novosibirsk Extended Abstr 1, pp. 308–310

Larson RL (1991) Geological consequences of superplumes. Geology 19: 963–966

Lorenz V, Kurszlaukis S, Stachel T, Brey GP, Stanistreet IG, Franz L (1995) Volcanology of the diatreme-rich carbonatitic Gross Brukkaros Volcanic Field and the near-by Gibeon Kimberlite

Province, Namibia(abstract). In: Sixth Int Kimberlite Conf, Novosibirsk Extended Abstr 1, pp 333–335
Luth RW, Virgo D, Boyd FR, Wood BJ (1990) Ferric iron in mantle derived garnets, implications for thermobarometry and the oxidation state of the mantle. Contrib Mineral Petrol 104: 56–72
MacGregor ID (1975) Petrologic and thermal structure of the upper mantle beneath South Africa in the Cretaceous. Phys Chem Earth 9: 455–466
Mitchell RH (1984) Garnet lherzolites from the Hanaus-I and Louwrensia kimberlites of Namibia. Contrib Mineral Petrol 86: 178–188
Nickel KG (1989) Garnet-pyroxene equilibria in the system SMACCR (SiO_2-MgO-Al_2O_3-CaO-Cr_2O_3): The Cr-geobarometer. Spec Publ Geol Soc Aust 14: 901–912
Nicolas A, Achauer U, Daignieres M (1994) Rift initiation by lithospheric rupture. Earth Planet Sci Lett 123: 281–298
O'Neill HStC (1980) An experimental study of Fe-Mg-partitioning between garnet and olivine and its calibration as a geothermometer: corrections. Contrib Mineral Petrol 72: 337
O'Neill HStC, Wood BJ (1979) An experimental study of Fe-Mg-partitioning between garnet and olivine and its calibration as a geothermometer. Contrib Mineral Petrol 70: 59–70
Pavoni N (1993) Pattern of mantle convection and Pangea breakup, as revealed by the evolution of the African plate. J Geol Soc London 150: 953–964
Pearson DG, Boyd FR, Hoal KEO, Hoal BG, Nixon PH, Rogers NW (1994) A Re-Os isotopic and petrological study of Namibian peridotites: contrasting petrogenesis and composition of on- and off-craton lithospheric mantle. Mineral Mag 58A: 703–704
Pollack HN, Chapman DS (1977) On the regional variation of heat flow, geotherms, and lithospheric thickness. Tectonophysics 38: 279–296
Sabadini R, Doglioni C, Yuen DA (1990) Eustatic sea level fluctuations induced by polar wander. Nature 345: 708–710
Sabadini R, Giunchi C, Gasperini P, Boschi E (1992) Plate motion and dragging of the upper mantle: lateral variations of lithospheric thickness and their implications for intraplate deformation. Ann Geophys 10 Suppl 1: C83
Smith CB (1983) Pb, Sr and Nd isotopic evidence for sources of Southern African Cretaceous kimberlites. Nature 304: 51–54
Sobolev NV (1977) Deep-seated inclusions in kimberlites and the problem of the composition of the upper mantle (transl Russian edn, 1974). Am Geophys Union, Washington,
Sobolev NV, Lavrent'ev YuG, Pokhilenko NP, Usova LV (1973) Chrome-rich garnets from the kimberlites of Yakutia and their parageneses. Contrib Mineral Petrol 40: 39–52
Spriggs AJ (1988) An isotopic and geochemical study of kimberlites and associated alkaline rocks from Namibia. PhD thesis, Univ Leeds, England
Stachel T, Lorenz V, Stanistreet G (1994) Gross Brukkaros (Namibia) – an enigmatic crater fill reinterpreted as due to Creataceous caldera evolution. Bull Volcanol 56: 386–397
Wilson JT (1963) Evidence from islands on the spreading of the ocean floor. Nature 197: 536–538